Dielectric dispersion of BaSrTiO3 thin film from centimeter to submillimeter wavelengths

Grégory Houzet, Karine Blary, Sylvie Lepilliet, Didier Lippens, Ludovic Burgnies, Gabriel Vélu, Jean-Claude Carru, Edwin Nguema Agnandji, Patrick Mounaix

Journal of Applied Physics

Dielectric dispersion of $BaSrTiO_3$ thin film from centimeter to submillimeter wavelengths

Cite as: J. Appl. Phys. **109**, 014116 (2011); https://doi.org/10.1063/1.3531534
Submitted: 09 July 2010 • Accepted: 24 November 2010 • Published Online: 14 January 2011

Gregory Houzet, Karine Blary, Sylvie Lepilliet, et al.

Dielectric dispersion of $BaSrTiO_3$ thin film from centimeter to submillimeter wavelengths

Gregory Houzet,[1] Karine Blary,[1] Sylvie Lepilliet,[1] Didier Lippens,[1,a)] Ludovic Burgnies,[2,b)] Gabriel Vélu,[2] Jean-Claude Carru,[2] Edwin Nguéma,[3] and Patrick Mounaix[3,c)]
[1]*Institut d'Électronique de Microélectronique et de Nanotechnologie, UMR CNRS 8520, Université de Lille 1, 59652 Villeneuve d'Ascq cedex, France*
[2]*Laboratoire d'Etude des Matériaux et Composants pour l'ELectronique, Université du Littoral Côte d'Opale, 62228 Calais cedex, France*
[3]*Centre de Physique Moléculaire et Hertzienne, UMR 5798, Université de Bordeaux 1, 33405 Talence cedex, France*

(Received 9 July 2010; accepted 24 November 2010; published online 14 January 2011)

The dielectric dispersion of ferroelectric $Ba_xSr_{1-x}TiO_3$ (BST) thin film in a paraelectric phase was characterized from centimeter to submillimeter wavelengths. To this aim, interdigitated capacitors were patterned on a micrometer scale onto a BST layer with a barium concentration of 0.5 and were subsequently integrated by using a coplanar waveguide technology. The retrieval of the complex permittivity of BST was performed by vectorial scattering parameter measurements up to 190 GHz for various controlling dc field up to 300 kV/cm. At higher frequency, submillimeter wavelength measurements were performed by time domain spectroscopy under free space condition. On this basis, the dispersion of the real part of the permittivity along with the loss tangent are retrieved in agreement with a distributed interaction of ac-field with soft phonons vibration modes, and overlapping between dipole polarization and ionic polarization is observed, around 700 GHz. It is also shown that dipole polarization can be attributed to the presence of small polar nanoregions in the BST film which act as in ferroelectric material with diffuse phase transition. © *2011 American Institute of Physics*. [doi:10.1063/1.3531534]

I. INTRODUCTION

During the past decades, the number of applications using ferroelectric materials has dramatically increased owing to technological advances. For agile microwave components,[1–3] tunability and miniaturization are reached with a ferroelectric material giving a high permittivity (κ) value and a voltage-control of the dielectric constant.[4–6] Good material candidates are $BaTiO_3$ (BT) based materials, and especially the $Ba_xSr_{1-x}TiO_3$ (BST) with a barium concentration $x \sim 0.5–0.6$ giving high permittivity and significant tunability at room temperature. It is well known that, above the Curie temperature, the paraelectric phase of BT-based materials permits one to obtain low dielectric losses at microwave and millimeter wavelengths.[7] Moreover, a lowering of overall losses of components can be achieved by deposing the material in thin film with thickness around hundreds of nanometers. The counterpart is the degradation of dielectric properties compared to bulk materials (ceramics or crystals) with a permittivity decrease and losses increase, principally due to defects in the film.[8] If real part value of the permittivity can be correlated intrinsically to the eigenfrequencies of the optical phonon mode in bulk or thin film materials, the loss mechanisms are more complicated to analyze and depend notably on deposition conditions. In bulk materials, the main intrinsic mechanisms in BST deal with the ac-field interaction with phonon modes in three- or more intricate four-quantum mechanisms. Quasi-Debye mechanisms can also exist under some assumptions.[9] In paraelectric phase, the latter can emanate mainly from dc bias but also from a distribution of local remanent polarizations induced by defects.[9]

From a structural point of view, relaxation phenomena can originate from various mechanisms. Arlt *et al.*[10] have shown that the emission of sound waves from the vibrating domain wall gives a dielectric dispersion with a Debye-type relaxation at microwave frequencies. Some authors have studied others mechanisms like piezoelectric resonance of the domains, the grain stress, and the inertia of the grain boundaries,[11] and the influence of grain and domain sizes.[12] In particular, by decreasing the grain size it was shown that domain size decreases as well, and ferroelectric BT can approach a single domain state.[11] One could make profit of such a single domain state to obtain a high frequency relaxation for microwave applications. Localized microwave resonances in $SrTiO_3$ thin films and local dielectric response of $BaSrTiO_3$ have been pointed out by time-resolved confocal scanning optical microscopy measurements.[13,14] These experiments show the presence of ferroelectric polar nanodomains. Large ferroelectric domains appear under dc electric field ($E_{dc} \neq 0$) when nanodomains coalesce. Without dc electric field ($E_{dc}=0$), ferroelectric nanodomains of uniform size seem to be randomly placed in matrix, and large-scale domain motion is not expected. Each nanodomain can be modeled by a Debye relaxation with a proper characteristic time. In order to take into account the broadening distribu-

a)Electronic mail: didier.lippens@iemn.univ-lille1.fr.
b)Electronic mail: ludovic.burgnies@univ-littoral.fr.
c)Electronic mail: p.mounaix@cpmoh.u-bordeaux1.fr.

tion of the phase angle of ferroelectric nanodomain, a modified form of Debye relation is however needed.[14]

Moreover, Raman studies show the existence of polar nanoregions (PNRs) in BST films with a broadening of the phase transition at the Curie temperature and soft modes hardening as consequences.[15] This was confirmed by the conservation of bulk properties in sliced ferroelectric crystal[16] which attests that loss mechanisms in films do not depend on size effects but originate from the presence of defects in the material. The size of PNRs is of prime importance in the dielectric response of ferroelectric films, and those with diffuse phase transition (DPT)-ferroelectric with smaller PNR size than relaxors yield lower relaxation time.[17] In such a case, dispersions by dipole polarization from PNR, and by ionic polarization from soft phonon modes, can overlap at a few 100 GHz. In this context, dielectric spectroscopy over a broadband greatly helps the analysis of the loss mechanisms. Recently, some authors have predicted the aforementioned overlapping for BST ceramics by the analysis of microwave measurements below a few gigahertz (GHz) and IR-reflectivity in the terahertz (THz) spectral region. However, experimental data at intermediate frequencies namely at millimeter wavelengths are missing.[18] In order to have a comprehensive study of the dispersion characteristic of ferroelectric thin films notably at millimeter wavelengths, we propose here a complementary study by analyzing the dielectric dispersion of $Ba_{0.5}Sr_{0.5}TiO_3$ films deposited by a sol-gel technique from GHz frequency range up to 190 GHz, with additional THz measurements. We show first how the intrinsic properties of interdigitated capacitance (Sec. II), voltage-controlled with moderate electric field values, are deduced from the scattering parameters (Sec. III) by means of de-embedding techniques. Notably, this study points out "apparent" resonant effects which result from the finger capacitor scheme. We then address directly the dispersion of the complex permittivity retrieved (Sec. IV) from the propagation properties of coplanar transmission lines (TLs). The results of the THz measurements are reported in Sec. V while an analysis of dipole polarization is reported in Sec. VI.

II. DESIGN RULES AND FABRICATION

$Ba_{0.5}Sr_{0.5}TiO_3$ films were first deposited onto a sapphire substrate by a sol-gel technique. The precursor solutions for the BST were prepared by a sol-gel method using barium acetate $[Ba(CH_3COO)_2]$, strontium acetate $[Sr(CH_3COO)_2]$, and titanium (IV) isopropoxide $[Ti(C_4H_9O)_4]$ as starting materials. The solution in the proportion of Ba:Sr=50:50 was obtained for the film deposition by solving the precursors of barium and strontium into acetic acid at 100 °C during 1 h and adding titanium precursor, diluted in a hot alcohol (isopropanol), at 80 °C. After 2 h, the precursor solution was cooled down to the room temperature before a spin coating process was used to fabricate the films. The spin coating process was repeated until a nominal film thickness of 500 nm was achieved. Crystallinity was achieved via postdeposition annealing at 750 °C for 1 h in ambient air. Further details about the films deposition can be found elsewhere.[19]

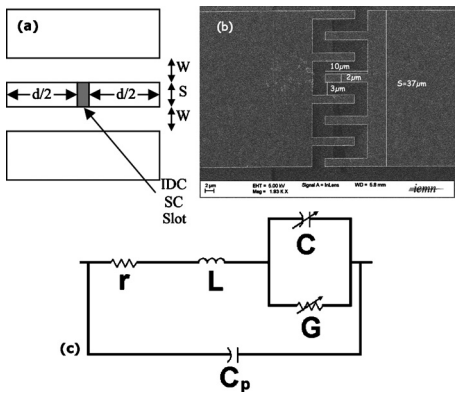

FIG. 1. CPW and IDC structures for de-embedding techniques (a), optical view of an IDC (b), and RLC equivalent circuit (c).

The film was characterized for structural properties. X-ray diffraction, using a Cu K_α radiation, was employed to assess film crystal quality and phase formation. X-ray diffraction patterns have indicated that films were crystallized into a pure perovskite structure, and have shown nontextured polycrystalline structures. A scanning electron microscopy was employed to assess surface morphology. The plan-view has shown a dense film without cracks. Its surface was smooth with a grain size average of about 50 nm.

For the fabrication of the devices aimed at operating rf, microwave, and millimeter wavelength measurements, interdigitated capacitors (IDCs), and coplanar waveguides (CPWs) were patterned by electron beam lithography in a polymethyl methacrylate electronic resist followed by Ti/Au deposition onto the BST film, by means of a lift-off technique. A typical pattern is shown in Fig. 1(a).

The slots of CPWs have a width $W=40$ μm and a central strip $S=37$ μm with length $d/2=100$ μm or $d/2=200$ μm. The gray zone in Fig. 1(a) corresponds to the location of an IDC or a short circuit (SC). Indeed as seen later, some test devices with SCs are necessary for de-embedding techniques with $d/2=100$ μm and $d/2=200$ μm while a third structure with the IDC and $d/2=100$ μm permits to retrieve the complex permittivity of BST film. A photograph of an IDC is given in Fig. 1(b). For wide band measurements, the finger width is $w=2$ μm for a finger spacing of $e=3$ μm and a finger length of $\ell=10$ μm. These dimensions were chosen to have a low capacitance value about 50 fF to reject the resonant behavior of the IDC out of the millimeter wave range. Moreover the thickness of sapphire substrate was limited to 300 μm to shift the occurrence of substrate modes above 200 GHz. Another IDC layout was also patterned with finger spacing $e=1$ μm and $\ell=8$ μm to reach about 50% of tunability at 30 V dc bias.

The intrinsic values of IDC were measured by means of two de-embedding analysis, which were found suitable for specific frequency ranges. They were termed M and Y de-embedding techniques (see Appendix). Both analysis take into account (i) the $d/2$ lengths of coplanar lines, and (ii) the slight impedance mismatch between the characteristic impedance of CPWs and the 50 Ω reference impedance of the measurement setup. In addition, the M technique subtracts

the error terms introduced by the transition between CPW and the probe setup which impact the measurement accuracy in the high frequency range. In counterpart the M de-embedding gives incorrect capacitance and Q factor values in the lower part of microwave range.[20] The M (Y) de-embedding technique will retrieve the capacitance C_M (C_Y) and the quality factor Q_M (Q_Y) values of IDCs.

The measurements were performed (i) with a *impedance analyzer* (HP 4284 A) in the frequency range 100 Hz–1 MHz, (ii) with a vector analyzer (Agilent 8510C XF) from 100 MHz to 110 GHz, and (iii) with WR05 Oleson heads driven by a vector analyzer (Rohde & Schwarz ZVA24) from 140 to 220 GHz. Prior to measurements, calibration procedures were performed as follows: (i) by open circuit and SC below 1 MHz, and (ii) by LRRM technique (Line Reflect Match) above 100 MHz.

In the THz spectral region (0.2–3 THz), the BST films were characterized by conventional time domain spectroscopy (TDS) technique under free space conditions. While a thin film technology is a definite advantage for planar devices such as IDCs and CPWs, it is worth-mentioning that the characterization of thin film less than 1 μm raises a number of difficulties in a time domain analysis under front side illumination. First of all, a high mismatch is, in particular, achieved between air and the high κ ferroelectric film under test. In this case, the THz beam experiences multiple strong reflections at the input and within the sample. These difficulties are particularly troublesome in the upper part of the THz spectrum, due to a degradation of the signal-to-noise ratio. In the lower part of the spectrum, namely, around 100 GHz, another difficulty stems from the fact that the ac-probing field, radiated in free space, is $E \sim dJ/dt$ where J is the conduction current flowing in the radiating elements. At microwave frequencies, the subsequent decrease in the radiated power along with the increase in the operating wavelength dramatically weakens the interaction of the ac-field with the thin BST sample. All these limitations, in connection with mismatch, finite thickness, and nonuniform spectral density yielded a meaningful band of interest over one decade between 0.2 and 3 THz.[21]

III. SCATTERING MEASUREMENTS

The intrinsic capacitance and the inverse of the quality factor (Q^{-1}) corresponding to loss tangent of an IDC (see the dimensions in the previous section) which were measured with the M and Y de-embedding techniques, respectively, are plotted in Fig. 2 as a function of frequency from 100 MHz to 190 GHz. The M de-embedding technique yields a decrease in the capacitance around 50 fF while the Y method shows steepest variations. Above 100 GHz there is clearly a resonant feature pointed out by the M-method.

In the lower part of the spectrum, it can be checked that the C_Y decrease results from the error terms (matrix X in Appendix) which are not taken into account by Y de-embedding. Actually, for Y de-embedding the X-matrix is treated as a symmetric impedance mismatch while the M de-embedding shows that an asymmetric, and more complicated, mismatch exists. On the other hand, it can be noticed

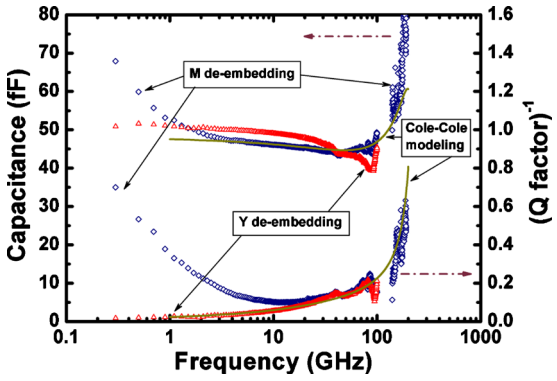

FIG. 2. (Color online) Capacitance and Q^{-1} factor of the IDC measured with M (diamond points) and Y (triangular points) de-embedding techniques, and modeled by Cole–Cole function (solid line).

that Q_Y and Q_M frequency dependences agree very well between 30 and 110 GHz while below 30 GHz only Q_Y must be regarded. From the comparison between both methods it can be concluded that C_M and Q_M with Q_Y give the full frequency behavior of IDCs.

IV. RETRIEVAL TECHNIQUES FOR THE DIELECTRIC DISPERSION

In the upper frequency range, the resonant feature can be analyzed by a *RLC* equivalent circuit given in Fig. 1(c). The capacitive element C which is frequency dependent describes the dispersion of BST films. On the other hand the dielectric dispersion due to dipole polarization can be analyzed by various empirical expressions.[18,22] In the present work we used the Cole–Cole function

$$\varepsilon^*(\omega) = \varepsilon' - j\varepsilon'' = \varepsilon'_\infty + \frac{\varepsilon^*_s - \varepsilon'_\infty}{1 + (i\omega\tau)^\beta}, \quad (1)$$

where ε'_∞ and ε^*_s are the relative permittivity at high and low frequencies (quasistatic permittivity value), respectively while $\omega_\tau = 1/\tau$ corresponds to the soft-mode eigenfrequency. The exponent $0 < \beta < 1$ is used to take into account the distribution of the ac-field interaction with soft-phonon mode. The quasistatic permittivity was obtained by low frequency measurements at 1 kHz and subsequent analysis by conformal mapping[23] ($\varepsilon^*_s = 360 - 4.5i$). The value of permittivity at high frequency (operating frequency $\omega \gg \omega_\tau$) can be estimated as $\varepsilon'_\infty = 5.4$.[24] A relaxation time $\tau = 0.21$ ps and an exponent value $\beta = 0.6$ can be estimated by fitting the scattering parameters from CPW measurements by means of full wave analysis [high frequency structure simulator (HFSS)-Ansoft].[20] As expected the relaxation time τ of the BST film is lower than one of BST ceramics with a soft-mode frequency 11.1 cm^{-1} in room temperature.[18]

A parasitic capacitance $C_p = 7$ fF was determined by the measurement of a CPW structure without IDC (slot of 13 μm length in the middle of the central strip). In order to illustrate the other equivalent lumped elements notably the inductive part, we plotted in Fig. 3 the current density maps calculated at 15 GHz and 180 GHz, respectively, by full wave analysis. At 15 GHz [Fig. 3(a)], an almost uniform repartition of the current over the cross section can be noted.

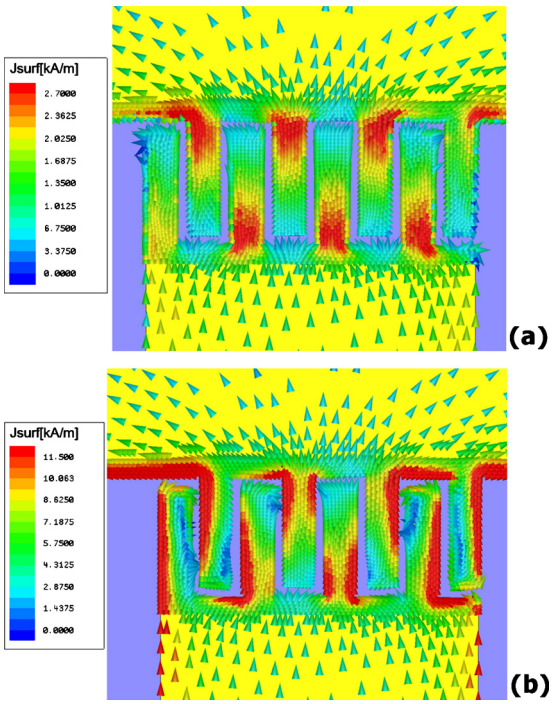

FIG. 3. (Color online) Mapping of current densities around an IDC at 15 (a) and 180 GHz (b).

Only half length of each finger participates to inductive and resistive behaviors of IDC. Besides, lower current densities flowing through the two boundary fingers at the right and left hand sides of IDC means that these fingers have a lower inductive contribution. As a consequence in a first approximation it is reasonable to consider only the contribution of three and a half fingers of length 10 μm. An equivalent inductance of IDC can be calculated as[25]

$$L = 3.5 \times \frac{\mu_0 \ell}{2\pi}\left\{ a\,\sinh(x) + (x)a\,\sinh(x^{-1}) + \frac{1}{3x} - \frac{1}{3}x^2[(1+x^{-2})^{3/2} - 1]\right\}, \quad (2)$$

with $x=\ell/(w+t)$, and the equivalent resistance by

$$r = \frac{1}{4}\frac{1}{\sigma}\frac{\ell}{wt}, \quad (3)$$

where ℓ, w, and $t=0.5$ μm are the length, width, and thickness of a finger, respectively. With a conductivity $\sigma=33.1\times10^6$ S/m,[2] we obtain $L=19$ pH and $r=86$ mΩ. These values were used as initial fitting parameters of C_M and Q factor measured from 100 MHz up to 190 GHz.

For the best fit (L, r, and C_p in Table I) the frequency dependence of C and Q^{-1} factor calculated by equivalent circuit compared with the dielectric dispersion by dipole polarization is reported in Fig. 2. Compared to the experimental data, the equivalent circuit frequency variations show a lower resonant feature above 170 GHz which can be attributed to a more pronounced inductive behavior of fingers at higher frequency which is not introduced in the equivalent circuit. Indeed, due to skin effect current passes along finger edges and each finger can act as two separate inductances [Fig. 3(b)]. Despite the fact that the current distribution varies continuously from the one corresponding to Fig. 3(a) to Fig. 3(b), one can evaluate the maximum frequency where the equivalent circuit of IDC is valid by equaling $t=2\delta$ with the skin thickness

$$\delta = \sqrt{\frac{2}{\omega\mu_0\sigma}}. \quad (4)$$

We obtain a maximum frequency $F_{max}=122$ GHz in accordance with the frequency for which disagreements can be observed in Fig. 2.

TABLE I. Parameter values for dielectric dispersion by dipole polarization and elements of the equivalent circuit of IDC.

ε_s^*	ε'_∞	τ (ps)	β	L (pH)	r (mΩ)	C_p (fF)
$360-4.5i$	5.4	0.21	0.6	13	80	7

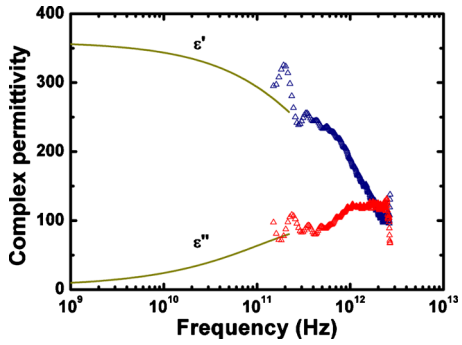

FIG. 4. (Color online) Complex permittivity as a function of frequency modeled by Cole–Cole function (solid lines) and measured by TDS (triangular points).

V. TERAHERTZ MEASUREMENTS

In practice, the TDS-THz measurements were performed with an unstructured BST thin film of thickness 0.5 μm deposited onto a 500 μm sapphire substrate. Details about the extraction of the frequency dependence of the complex permittivity on the basis of transmission measurements can be found elsewhere.[21] The variations versus frequency of the real part (ε') and of the imaginary part (ε'') are displayed in Fig. 4 from 0.14 to 3 THz. For a comparison with the previous results achieved at centimeter and long wave millimeter wave (30–190 GHz), the frequency dependence of the Cole–Cole function (1) using the material parameters reported in Table I was also plotted. Below about 200 GHz a large discrepancy between the analytical (Cole–Cole) and retrieved complex permittivity values can be noticed. The disagreement can be mainly explained by the ultrashort scattering length (0.5 μm) of the sample illuminated under normal incidence. In contrast a good fit is noted between 0.2 and 0.8 THz with notably comparable slope. Above 800 GHz, the real part of the permittivity decreases steeper with a concomitant further increase in the imaginary part which can be explained by the occurrence ionic polarization effects. This overlapping between dipole polarization and ionic polarization was previously observed at lower frequency in BST

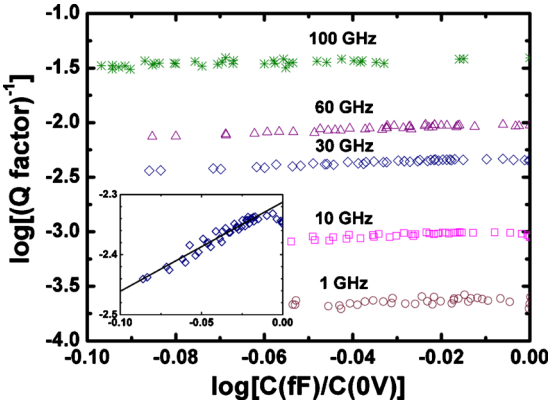

FIG. 5. (Color online) Log-log representation of Q^{-1} factor vs capacitance with frequency as a parameter, and measured at room temperature. The inset shows an expanded representation at 30 GHz.

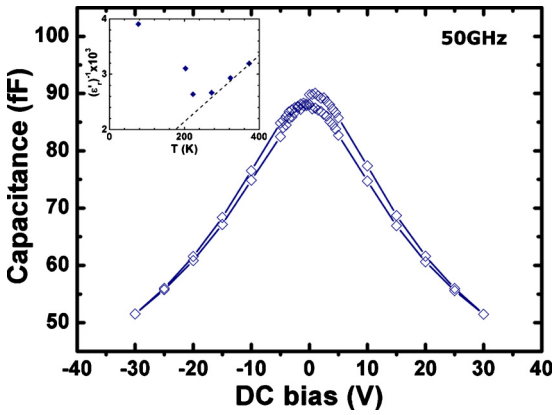

FIG. 6. (Color online) Capacitance-voltage characteristic measured at 50 GHz and at room temperature. The inset shows the inverse of permittivity as a function of temperature.

ceramics.[18] It is believed that the shift to higher frequency range observed here for BST thin films can be first explained by the "hardening" of soft phonon modes. Second, it can be analyzed as a reduction of PNRs which act as in DPT-ferroelectric in our BST film.

VI. ANALYSIS OF DIPOLE POLARIZATION

For this analysis we consider the experimental data achieved with a voltage control of the tunable capacitance. We show in Fig. 5 the variations in Q^{-1} factor versus capacitance plotted in logarithmic scales by taking the measurement frequency as a parameter. To prevent dc-field-induced quasi-Debye mechanism which could be preponderant in BST in paraelectric phase,[9] the dc electric field was limited to $E_{dc} < 100$ kV/cm.

At each frequency between 1 and 100 GHz, the Q^{-1} factor as a function of the voltage-controlled capacitance shows similar variations. For a more quantitative analysis the inset of Fig. 5 represents an expanded plot at 30 GHz. From this plot, it is shown that the Q^{-1} factor increases with capacitance according to a power law $Q^{-1}=(\varepsilon')^n$ with $n\#1.5$. Such a law is characteristic of ac-field interaction with soft phonons, or similarly with local polar regions as predicted for bulk BST.[26] If in bulk BST, such polar regions originate from a compositional heterogeneity, oxygen vacancies seem to be the main cause in BST thin films.[27] Also it was demonstrated that microwave losses and dielectric relaxation can depend strongly on defect concentration.[27] On this basis, the dielectric dispersion we measured at millimeter frequency range and below can be attributed to the presence of PNRs due to oxygen vacancies.

This conclusion is corroborated by the plot in Fig. 6 of the *C-V* curve, measured at 50 GHz and at room temperature, for an IDC with a 1 μm finger spacing. In inset we also plotted the temperature dependence of ε^{-1} at 0 V dc bias. A linear increase in ε^{-1} above 273 K agrees with the Curie–Weiss law for paralectric materials. In addition, a broader and flatter permittivity peak near the Curie temperature ($T_C \sim 250$ K) than for bulk BST can be explained by the existence of PNRs as in ferroelectric relaxors[28] or DPT-ferroelectrics. It is known that in relaxors the permittivity peak temperature (T_m) increases at increasing frequency.[29] Because no frequency dependence of T_m is available from the present experimental work, it seems difficult to determine precisely by this way what the process is in our BST film. On the other side, relaxors is a slow process with a dielectric relaxation around 100 MHz. Such a relaxation was not observed in previous frequency measurements and can be discarded. Finally, in the C-V curve of Fig. 6 while the BST film is in paraelectric phase at room temperature, a very weak hysteresis persists and confirms the presence of PNRs.

VII. CONCLUSION

The dielectric dispersion of $Ba_{0.5}Sr_{0.5}TiO_3$ thin films at microwave, millimeter, and submillimeter wavelengths was characterized experimentally. De-embedding and inversion (material parameter retrieval) techniques allowed us to characterize the dipole polarization relaxation mechanisms over an ultrawide frequency band. An overlap between the dipole and ionic polarizations was also expected for frequencies around 700 GHz. The high frequency value found here was attributed to small PNRs within the BST film which thus behaves as a ferroelectric material with DPT. These results are in agreement with the previous observations of Tsurumi *et al.*[17] for a BST ceramic. At higher frequency, the beginning of a relaxation by ionic polarization is observed near the THz domain.

APPENDIX

1. M DE-EMBEDDING TECHNIQUE

The M de-embedding technique needs two CPWs of lengths L and 2L in addition to a structure with an IDC located in the middle of a CPW of total length 2L. Scattering parameters of CPW lines were measured and written as transfer matrixes

$$M_i = \frac{1}{S_{21}^i}\begin{bmatrix} -\det S^i & S_{11}^i \\ -S_{22}^i & 1 \end{bmatrix},$$

with $i=1$ or 2 for CPW of length $d_1=L$ or $d_2=2L$, respectively.

Each transfer matrix can be decomposed in three matrixes $M_i = X \cdot L_i \cdot Y$, where X and Y represent the access boxes in port 1 and 2, respectively,[30] and

$$L_i = \begin{bmatrix} \lambda_i & 0 \\ 0 & \lambda_i^{-1} \end{bmatrix},$$

is the transfer matrix of a perfectly matched TL with $\lambda_i = \exp(-\gamma d_i)$ and where $\gamma = \alpha + i\beta$ is the complex propagation constant of the TL.

By combining M_1 and M_2 we obtain an eigenvalue equation

$$M.X = X.L_1,$$

with $M = M_2 \cdot [M_1]^{-1}$ and $L_2[L_1]^{-1} = L_1$. The eigenvalues give the complex propagation constant of the TL, and eigenvectors, which are the columns of matrix X, give

$$A = \frac{X_{11}}{X_{21}} = \frac{M_{12}}{\lambda_1 - M_{11}} = \frac{\lambda_1 - M_{22}}{M_{21}},$$

$$B = \frac{X_{22}}{X_{12}} = \frac{M_{21}}{\lambda_1^{-1} - M_{22}} = \frac{\lambda_1^{-1} - M_{11}}{M_{12}}.$$

On the other hand, CPW with an IDC can be written as $M_C = X \cdot L_1 \cdot C \cdot L_1^{-1}$ (with C of the M_C matrix and 1 of the L one put in index), with C the transfer matrix of the serial IDC admittance $Y_{IDC} = G + iC\omega = y/Z_0$

$$C = \begin{bmatrix} 1 - 2y & 2y \\ -2y & 1 + 2y \end{bmatrix},$$

and M_C the transfer matrix of the CPW with an IDC measurements.

By combining M_C and M_2 matrixes, we obtain a second eigenvalue equation

$$Q \cdot X = X \cdot L_1 \cdot C \cdot L_1^{-1},$$

with $Q = M_C \cdot M_2^{-1}$. Developing this eigenvalue equation and dividing by appropriate X_{21} or X_{12} term, we obtain a set of four equations

$$(Q_{11} - 1) \cdot A + Q_{12} = -2y \cdot (A + D), \tag{5}$$

$$(Q_{11} - 1) + Q_{12} \cdot B = 2y \cdot \frac{(A + D)}{D}, \tag{6}$$

$$Q_{21} \cdot A + (Q_{22} - 1) = -2y \cdot (1 + B \cdot D), \tag{7}$$

$$Q_{21} + (Q_{22} - 1) \cdot B = 2y \cdot \frac{(1 + B \cdot D)}{D}, \tag{8}$$

where y and $D = X_{12}/X_{21} \cdot \lambda_1^{-2}$ are unknown.

From Eqs. (5) and (6), we calculate

$$D = -\frac{(Q_{11} - 1) \cdot A + Q_{12}}{(Q_{11} - 1) + Q_{12} \cdot B}, \quad \text{and}$$

$$y = -\frac{1}{2}\frac{A + D}{(Q_{11} - 1) \cdot A + Q_{12}} = \frac{1}{2D}\frac{A + D}{(Q_{11} - 1) + Q_{12} \cdot B},$$

and from Eqs. (7) and (8)

$$D = -\frac{Q_{21} \cdot A + (Q_{22} - 1)}{Q_{21} + (Q_{22} - 1) \cdot B}, \quad \text{and}$$

$$y = -\frac{1}{2}\frac{1 + B \cdot D}{Q_{21} \cdot A + (Q_{22} - 1)} = \frac{1}{2D}\frac{1 + B \cdot D}{Q_{21} + (Q_{22} - 1) \cdot B}.$$

In general, the two admittance values are different because of the dissymmetry in the parameters of the matrix X (access box) which take into account overall error terms introduced by the transition between CPW and probe setup. However, if a simpler mismatch alone is assumed the two admittance values converge to the y values calculated by Y de-embedding below.

2. Y DE-EMBEDDING TECHNIQUE

The Y de-embedding technique needs a CPW of length 2L in addition to a structure with an IDC located in the middle of a CPW of total length 2L. Scattering parameters are written as admittance matrixes

$$Y^T = \begin{bmatrix} Y_{11}^T & Y_{12}^T \\ Y_{21}^T & Y_{22}^T \end{bmatrix}, \quad \text{for TL-CPW, and}$$

$$Y^C = \begin{bmatrix} Y_{11}^C & Y_{12}^C \\ Y_{21}^C & Y_{22}^C \end{bmatrix} \quad \text{for CPW loaded by an IDC.}$$

By assuming the simpler case of a mismatch alone between the CPW and probe setup, we can calculate

$$Y_{12}^T = Y_{21}^T = -\frac{Y_0}{\sinh(2\gamma L)}, \quad \text{and}$$

$$Y_{12}^C = Y_{21}^C = -\frac{2Y_0}{2\sinh(2\gamma L) + z[1 + \cosh(2\gamma L)]},$$

with $Y_0 = 1/Z_0$.

The equality between Y_{12} and Y_{21} is theoretical and depends on the calibration setup used before the microwave and millimeter wavelengths measurements (short-open-load-thru, line-reflect-match, and so on). These experimental different Y_{12} and Y_{21} values will result in two admittance values of IDC as in the M de-embedding technique.

Complex propagation constant term $\sinh(2\gamma L)$ is determined from $Y_{12}^T = Y_{21}^T$ and the admittance $Y_{IDC} = G + iC\omega = y/Z_0$ of the IDC can be calculated as

$$y = \frac{1}{2}\frac{Y_{12}^T Y_{12}^C}{Y_{12}^T Y_{12}^C}[1 + \cosh(2\gamma L)], \quad \text{or}$$

$$y = \frac{1}{2}\frac{Y_{21}^T Y_{21}^C}{Y_{21}^T Y_{21}^C}[1 + \cosh(2\gamma L)].$$

A similar expression for the admittance y can be found in literature[31] without the propagation $\cosh(2\gamma L)$ term. Without this term, the admittance-frequency dependence shows an unrealistic resonance at much lower frequency than the IDC one, which limits the frequency range of this de-embedding technique.

[1]A. Marteau, G. Vélu, G. Houzet, L. Burgnies, E. Lheurette, J.-C. Carru, and D. Lippens, Appl. Phys. Lett. **94**, 023507 (2009).
[2]F. Ponchel, J. Midy, J. F. Legier, C. Soyer, D. Rémiens, T. Lasri, and G. Guéguan, J. Appl. Phys. **107**, 054112 (2010).
[3]J. H. Leach, H. Liu, V. Avrutin, B. Xiao, Ü. Özgür, H. Morkoç, J. Das, Y. Y. Song, and C. E. Patton, J. Appl. Phys. **107**, 084511 (2010).
[4]M. Ouaddari, S. Delprat, F. Vidal, M. Chaker, and K. Wu, IEEE Microw. Wirel. Compon. Lett. **53**, 1390 (2005).
[5]S. Delprat, M. Ouaddari, F. Vidal, M. Chaker, and K. Wu, IEEE Microw. Wirel. Compon. Lett. **13**, 211 (2003).
[6]X.-Y. Zhang, Q. Song, F. Xu, S. Sheng, P. Wang, and C. K. Ong, J. Phys. D: Appl. Phys. **42**, 065411 (2009).
[7]N. Setter, D. Damjanovic, L. Eng, G. Fox, S. Gevorgian, S. Hong, A. Kingon, H. Kohlstedt, N. Y. Park, G. B. Stephenson, I. Stolitchnov, A. K. Taganstev, D. V. Taylor, T. Yamada, and S. Streiffer, J. Appl. Phys. **100**, 051606 (2006).
[8]T. J. Jackson and I. P. Jones, J. Mater. Sci. **44**, 5288 (2009).
[9]K. F. Astafiev, A. K. Tagantsev, and N. Setter, J. Appl. Phys. **97**, 014106 (2005).
[10]G. Arlt, U. Bottger, and S. Witte, Appl. Phys. Lett. **63**, 602 (1993).
[11]M. P. McNeal, S.-J. Jang, and R. E. Newnham, J. Appl. Phys. **83**, 3288 (1998).
[12]M. J. Dalberth, R. E. Stauber, J. C. Price, T. Rogers, and D. Galt, Appl. Phys. Lett. **72**, 507 (1998).
[13]P. Irvin, J. Levy, J. H. Haeni, and D. G. Schlom, Appl. Phys. Lett. **88**, 042902 (2006).
[14]C. Hubert, J. Levy, E. J. Cukauskas, and S. W. Kirchoefer, Phys. Rev. Lett. **85**, 1998 (2000).
[15]D. A. Tenne, A. Soukiassian, M. H. Zhu, A. M. Clark, X. X. Xi, H. Choosuwan, Qi He, R. Guo, and A. S. Bhalla, Phys. Rev. B **67**, 012302 (2003).
[16]L. W. Chang, M. McMillen, F. D. Morrison, J. F. Scott, and J. M. Gregg, Appl. Phys. Lett. **93**, 132904 (2008).
[17]T. Tsurumi, J. Li, T. Hoshina, H. Kakemoto, M. Nakada, and J. Akedo, Appl. Phys. Lett. **91**, 182905 (2007).
[18]T. Teranishi, T. Hoshina, H. Takeda, and T. Tsurumi, J. Appl. Phys. **105**, 054111 (2009).
[19]G. Vélu, J. C. Carru, E. Cattan, D. Remiens, X. Melique, and D. Lippens, Ferroelectrics **288**, 59 (2003).
[20]G. Houzet, L. Burgnies, G. Vélu, J.-C. Carru, and D. Lippens, Appl. Phys. Lett. **93**, 053507 (2008).
[21]P. Mounaix, M. Tondusson, L. Sarger, D. Michau, V. Reymond, and M. Maglione, Jpn. J. Appl. Phys., Part 1 **44**, 5058 (2005).
[22]J. C. Booth, I. Takeuchi, and K.-S. Chang, Appl. Phys. Lett. **87**, 082908 (2005).
[23]S. S. Gevorgian, T. Martinsson, P. L. J. Linnér, and E. L. Kollberg, IEEE Trans. Microwave Theory Tech. **44**, 896 (1996).
[24]T. Ostapchuk, J. Petzelt, J. Hlinka, V. Bovtun, P. Kuzel, I. Ponomareva, S. Lisenkov, L. Bellaiche, A. Tkach, and P. Vilarinho, J. Phys.: Condens. Matter **21**, 474215 (2009).
[25]E. Pettenpaul, H. Kapusta, A. Weisgerber, H. Mampe, J. Luginsland, and I. Wolff, IEEE Trans. Microwave Theory Tech. **36**, 294 (1988).
[26]A. K. Tagantsev, V. O. Sherman, K. F. Astafiev, J. Venkatesh, and N. Setter, J. Electroceram. **11**, 5 (2003).
[27]T. Moon, B. Lee, T. Kim, J. Oh, Y. W. Noh, S. Nam, and B. Park, Appl. Phys. Lett. **86**, 182904 (2005).
[28]J. Li, H. Kakemoto, S. Wada, T. Tsurumi, and H. Kawaji, J. Appl. Phys. **100**, 024106 (2006).
[29]J. Xu, D. Zhou, W. Menesklou, and E. Ivers-Tiffée, J. Appl. Phys. **106**, 074107 (2009).
[30]L. Burgnies, G. Vélu, G. Houzet, K. Blary, J.-C. Carru, and D. Lippens, IEEE Trans. Instrum. Meas. **57**, 1127 (2008).
[31]J.-Y. Kim and A. M. Grishin, Appl. Phys. Lett. **88**, 192905 (2006).